

A Mechanism of Tropical Convection Inferred from Observed Variability in the Moist Static Energy Budget

HIROHIKO MASUNAGA

Hydrospheric Atmospheric Research Center, Nagoya University, Nagoya, Japan

TRISTAN S. L'ECUYER

Department of Atmospheric and Oceanic Sciences, University of Wisconsin–Madison, Madison, Wisconsin

(Manuscript received 23 January 2014, in final form 16 June 2014)

ABSTRACT

Temporal variability in the moist static energy (MSE) budget is studied with measurements from a combination of different satellites including the Tropical Rainfall Measuring Mission (TRMM) and A-Train platforms. A composite time series before and after the development of moist convection is obtained from the observations to delineate the evolution of MSE and moisture convergences and, in their combination, gross moist stability (GMS). A new algorithm is then applied to estimate large-scale vertical motion from energy budget constraints through vertical-mode decomposition into first and second baroclinic modes and a background shallow mode. The findings are indicative of a possible mechanism of tropical convection. A gradual destabilization is brought about by the MSE convergence intrinsic to the positive second baroclinic mode (congestus mode) that increasingly counteracts a weak MSE divergence in the background state. GMS is driven to nearly zero as the first baroclinic mode begins to intensify, accelerating the growth of vigorous large-scale updrafts and deep convection. As the convective burst peaks, the positive second mode switches to the negative mode (stratiform mode) and introduces an abrupt rise in MSE divergence that likely discourages further maintenance of deep convection. The first mode quickly dissipates and GMS increases away from zero, eventually returning to the background shallow-mode state. A notable caveat to this scenario is that GMS serves as a more reliable metric when defined with a radiative heating rate included to offset MSE convergence.

1. Introduction

Moist processes are crucial for the maintenance of tropical large-scale circulation that, in turn, conditions the local environment to be favorable or unfavorable for moist convection. A wide spectrum of ideas from simple conceptual theory to sophisticated cumulus parameterizations have been proposed to deal with those two-way processes central to tropical dynamics. As a simplest approach to this problem, Neelin and Held (1987) devised a way to reduce the intrinsic complexity to a tractable level by invoking the concept of gross moist stability¹

(GMS). GMS in its original form is equivalent to the vertically integrated horizontal divergence of moist static energy (MSE) divided by lower-tropospheric convergence. Variants of GMS have since been utilized extensively for different theoretical applications (e.g., Neelin and Yu 1994; Neelin and Zeng 2000; Sobel and Gildor 2003; Sobel and Neelin 2006; Raymond and Fuchs 2007, 2009; Sugiyama 2009a,b; Raymond et al. 2009).

Whereas GMS was originally intended as a positive constant prescribed to seek steady-state solutions, GMS is in theory applicable to time-dependent solutions. Raymond (2000) explored this direction and discussed the possibility of GMS being negative, in which case the system is subject to a positive feedback where an import of MSE would lead to heavier precipitation and thus further strengthen the MSE convergence (or conversely an MSE export would make a dry column even drier). A negative GMS was confirmed to take place during times when a self-sustaining growth of convection and large-scale vertical motion occurs in cloud-resolving model

¹ The term “gross moist stability” itself was first coined by Held and Hoskins (1985).

Corresponding author address: Hirohiko Masunaga, Hydrospheric Atmospheric Research Center, Nagoya University, Furocho, Chikusa-ku, Nagoya 464-8601, Japan.
E-mail: masunaga@hyarc.nagoya-u.ac.jp

simulations (Bretherton et al. 2005; Sessions et al. 2010). GMS is thus not an externally specifiable constant but a variable internal to the system itself (Kuang 2011). The temporal evolution of GMS as convection grows and decays, however, has yet to be verified against observational evidence.

In contrast to the widespread interests in theoretical and modeling studies, GMS has not received as much attention in observational work with a few notable exceptions based on reanalysis datasets (Yu et al. 1998; Back and Bretherton 2006; Peters et al. 2008). These authors, aware of the potential limitations in reanalysis data, compared multiple datasets from different sources and found tolerable but consistent disagreements among them. GMS is in the first place aimed at “summarizing our ignorance of the details of the convective and large-scale transients” (Neelin and Held 1987), which involve the processes that may be controlled by (or even built into) parameterized physics in the reanalysis data production. Genuine observations of GMS, on the other hand, are technically challenging. Satellite observations provide uniform soundings of the global atmosphere beyond the reach of ground networks, but no currently operational satellite sensor is capable of measuring the complete vertical profile of divergence from which GMS is calculated.

Meanwhile, Masunaga (2013) demonstrated that the vertically integrated moisture convergence and dry static energy (DSE) convergence could be estimated from satellite observations alone with the help of water and thermal budget constraints. This strategy is further extended in the present paper to yield a full vertical structure of large-scale mean divergence (and thus vertical velocity). A unique aspect of the current approach is that it avoids using the momentum equations to derive atmospheric vertical motion, relying instead largely on thermodynamic consideration. This offers a huge advantage for satellite data analyses, given that satellite remote sensing provides limited access to wind measurements but is a rich source of the thermodynamic variables such as air temperature, humidity, and precipitation (or vertically integrated condensational heating). The new approach proposed here opens a pathway to generating observationally based estimates of GMS fully independent of model parameterizations. This direction is also explored by Handlos and Back (2014), who developed a semiempirical approach to evaluating large-scale vertical motion by combining various satellite-based data products with reanalysis data.

The main objectives of this work are to provide an observational diagnosis of GMS with particular focus on its evolution over time and to discuss a plausible

mechanism of tropical convection as inferred from the observations. Following sections 2 and 3, which outline the data and method, analysis results are presented in section 4. A mechanism of tropical convection is discussed in light of the current findings in section 5, and concluding remarks are given in section 6.

2. Data

The data ingested into the analysis are summarized in this section. The *Aqua* Atmospheric Infrared Sounder and Advanced Microwave Sounder Unit (AIRS/AMSU, hereafter AIRS collectively) provide a cloud-cleared air temperature and water vapor mixing ratio in the level-2 AIRX2RET, version 5, dataset (Susskind et al. 2003, 2011). The *Aqua* Advanced Microwave Scanning Radiometer for Earth Observing System (AMSR-E) is employed for column water vapor (CWV) and sea surface temperature (SST) via the Remote Sensing Systems (RSS; Wentz and Meissner 2000), as well as for precipitation retrieved by the Goddard Profiling (GPROF) 2010 algorithm (Kummerow et al. 2001, 2011). The *CloudSat* Cloud Profiling Radar (CPR) 2B-CLDCLASS (Wang and Sassen 2001), 2B-FLXHR-lidar (L'Ecuyer et al. 2008; Henderson et al. 2013), and 2C-PRECIP-COLUMN (Haynes et al. 2009) products are used for cloud properties, the radiative heating rate, and precipitation-type identification, respectively. Near-surface wind vectors are obtained from the Quick Scatterometer (QuikSCAT) SeaWinds level-3 daily gridded data (Perry 2001). The *Aqua* and *CloudSat* satellites, both participating in the A-Train instrument constellation, have overpasses around 0130 and 1330 local time (LT). The QuikSCAT satellite had been flying around 0600 and 1800 LT until it ceased to operate in November 2009. Diurnal variations are expected to be statistically smeared out when averaged between the ascending and descending paths, with the exception of shortwave heating, which, being sampled at 1330 LT, overestimates the true daytime-mean solar radiation (section 5b). These sun-synchronous satellite observations are analyzed in combination with precipitating clouds detected by the Tropical Rainfall Measuring Mission (TRMM) Precipitation Radar (PR) level-2 products (TRMM PR Team 2005). TRMM is in a precessing orbit with a 47-day repeat cycle so the local time of TRMM observations changes from one orbit to another.

We adopt 13 pressure levels for this analysis (925, 850, 700, 600, 500, 400, 300, 250, 200, 150, and 100 hPa), in addition to levels at the surface and cloud base that are allowed to vary temporally and spatially. Cloud-base pressure p_{CB} is defined as the lifting condensation level

(LCL) determined from observations, and surface pressure is interpolated to AIRS footprints internally in the AIRS operational algorithm. The analysis covers the global tropical oceans (15°S–15°N) with continents and islands excluded. The analysis period spans 7 years from 1 December 2002 to 30 November 2009 with the exception of *CloudSat* data, which are only available beginning on 1 July 2006.

3. Method

a. Composite time series

The temporal evolution is constructed with a large number of sporadic satellite observations that are composited into a statistically continuous time series. The methodology is thoroughly described elsewhere (Masunaga 2012, 2013) and is not repeated here in great detail. A short summary of the analysis procedure may be outlined as follows. *CloudSat*, AIRS, and QuikSCAT measurements collected over a length of time are sorted in terms of the lead or lag time relative to the moment when TRMM detects precipitating clouds. Since the precessing TRMM orbit intersects other satellite overpasses at irregular time intervals, the overpass time difference drifts over time. The large collection of satellite measurements analyzed is eventually distributed continuously along the composite time axis and, when averaged in each hourly time bin, yields a statistical representation of the atmospheric variability prior and subsequent to the occurrence of moist convection.

The large-scale mean thermodynamic field is constructed from the cloud-cleared AIRS retrievals of temperature and humidity in combination with a semi-analytical estimate of the in-cloud sounding (Masunaga 2013). In the previous work, the composite analysis was separated into three cloud types—isolated cumulus clouds, moderately developed clouds, and highly organized systems—depending on the population density of TRMM-detected precipitation. We have tested the present method with these three types and found little qualitative difference, so in this paper only highly organized systems, defined when TRMM precipitation coverage exceeds 50% at time 0, are analyzed to avoid redundancy.

b. Free-tropospheric convergence of moisture and dry static energy

Following the method of Masunaga (2013), the moisture and DSE convergences integrated over the free troposphere (FT) are evaluated based on moisture and thermal budget considerations. Here, FT is defined as the whole tropospheric layer above cloud base, while

the layer below cloud base is referred to as the subcloud layer (SC). Moisture and DSE convergences are required for the vertical velocity estimates described later and the algorithm flow is briefly reviewed.

The moisture and thermal budget equations are

$$\begin{aligned} \frac{\partial q}{\partial t} + \mathbf{v} \cdot \nabla q + \omega \frac{\partial q}{\partial p} &= e - c, \\ \frac{\partial s}{\partial t} + \mathbf{v} \cdot \nabla s + \omega \frac{\partial s}{\partial p} &= L(c - e) + Q_R, \end{aligned} \quad (1)$$

These relations may be written in the flux form:

$$\begin{aligned} \frac{\partial q}{\partial t} + \nabla \cdot q\mathbf{v} + \frac{\partial q\omega}{\partial p} &= e - c, \\ \frac{\partial s}{\partial t} + \nabla \cdot s\mathbf{v} + \frac{\partial s\omega}{\partial p} &= L(c - e) + Q_R, \end{aligned} \quad (2)$$

where \mathbf{v} is the horizontal velocity vector, ω is the vertical p velocity, e is the reevaporation rate per unit mass, c is the condensation rate per unit mass, L is the specific latent heat of liquid water, and Q_R is the radiative heating rate per unit mass. Vertically integrating and horizontally averaging (2) with the horizontal convergence term split into the SC and FT, one obtains

$$-\overline{\langle \nabla \cdot q\mathbf{v} \rangle}_{\text{FT}} = \frac{\partial}{\partial t} \overline{\langle q \rangle} + \nabla \cdot [q(p_s)\mathbf{v}_{10}] \frac{\Delta p_{\text{SC}}}{g} - \overline{E} + \overline{P}_s \quad (3)$$

and

$$\begin{aligned} -\overline{\langle \nabla \cdot s\mathbf{v} \rangle}_{\text{FT}} &= \frac{\partial}{\partial t} \overline{\langle s \rangle} + \nabla \cdot [s(p_s)\mathbf{v}_{10}] \frac{\Delta p_{\text{SC}}}{g} - \overline{S} \\ &\quad - L\overline{P}_s - \overline{\langle Q_R \rangle}, \end{aligned} \quad (4)$$

where Δp_{SC} is the SC thickness, p_s is the surface pressure, \mathbf{v}_{10} is near-surface wind at 10 m above sea surface, and angle brackets denote vertical integrals:

$$\begin{aligned} \langle \dots \rangle &\equiv \int_{p_{\text{TP}}}^{p_s} \dots \frac{dp}{g}, \\ \langle \dots \rangle_{\text{FT}} &\equiv \int_{p_{\text{TP}}}^{p_{\text{CB}}} \dots \frac{dp}{g}, \end{aligned}$$

where the tropopause pressure p_{TP} is fixed at 100 hPa. The overbar indicates horizontal averaging over a circular large-scale domain with a radius of 100 km.

Each term on the right-hand sides of (3) and (4) is directly constrained by observations: the storage term is derived from a central difference to the composite time series, surface latent and sensible heat fluxes are obtained from the bulk formulas of Large et al. (1994), and surface precipitation and the radiative heating rate are

adopted from the AMSR-E and *CloudSat* data products, respectively. The SC convergence of moisture and DSE is computed with the AIRS sounding and scatterometer wind under the assumption that SC is well mixed over height dynamically and thermodynamically at all times. This assumption assures that q , s , and \mathbf{v}_{10} are each vertically homogeneous below cloud base, allowing the integral over SC to be expressed by near-surface variables alone, as found on the right-hand sides of (3) and (4). In general, q and s are known to be nearly vertically constant over tropical oceans (Johnson et al. 2001, and references therein). The SC wind is also relatively well mixed from the surface up to cloud base or roughly 500 m in height (Brümmer et al. 1974), although wind speeds averaged over the atmospheric boundary layer might be larger than $|\mathbf{v}_{10}|$ by 10%–20% (Stevens et al. 2002). In this work, no attempt is made to reconcile the difference between \mathbf{v}_{10} and the SC-mean wind since the discrepancy is generally small and there is no robust method to precisely offset the potential bias.

Uncertainties in the budget measurements are within a standard error of 1 W m^{-2} and a bias of approximately 35 W m^{-2} or less [see the appendix in Masunaga (2013)]. These values are small compared to the magnitude of moisture and DSE convergences during active convection and unlikely to introduce significant errors into the vertical velocity estimates described next. Along with the errors in the individual parameters listed above, other uncertainties may arise from limitations to the analysis methodology. An obvious limitation is that any vertical motion unaccounted for by a superposition of the three modes in consideration might not be properly reproduced. One might raise another concern that it has yet to be investigated further: how well the statistical time series averaged from sporadic snapshots over time represents the evolution of “real” convective systems. Such questions will be addressed in future work by reevaluating the results and methodology in light of in situ sounding array data.

c. Large-scale mean vertical velocity

Atmospheric water vapor rapidly decreases upward, while DSE increases with height toward the tropopause and beyond. The vertically integrated moisture convergence thus may be considered to mainly represent the lower-tropospheric convergence field, in contrast to DSE, which is more sensitive to the upper-tropospheric convergence. It follows that moisture and DSE convergence combined would provide a loose but useful observational constraint on the vertical structure of FT horizontal convergence (and hence of vertical velocity). To formulate this into a practical algorithm, the vertical profile of p velocity is expanded into a finite series of nondimensional basis functions $f_k(p)$ as

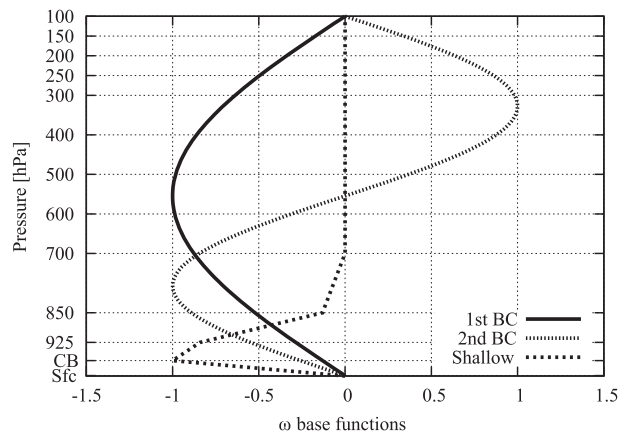


FIG. 1. Base functions of vertical velocity: first baroclinic mode (solid), second baroclinic mode (dotted), and shallow mode (dashed).

$$\bar{\omega}(p, t) = \bar{\omega}_{\text{bg}0}(p) + \sum_k \Omega_k(t) f_k(p),$$

where $\omega_{\text{bg}0}(p)$ is the time-independent background p velocity and $\Omega_k(t)$ is the expansion coefficient associated with the k th vertical mode. It is hereafter assumed that the temporal variability of $\bar{\omega}$ is accounted for by three basis functions consisting of first and second baroclinic modes, denoted by $f_{\text{bc}1}$ and $f_{\text{bc}2}$, respectively, and a shallow mode f_{shl} so that

$$\bar{\omega}(p, t) = \bar{\omega}_{\text{bg}0}(p) + \Omega_{\text{bc}1}(t) f_{\text{bc}1}(p) + \Omega_{\text{bc}2}(t) f_{\text{bc}2}(p) + \Omega_{\text{shl}}(t) f_{\text{shl}}(p). \quad (5)$$

The two baroclinic modes are each prescribed simply by a sinusoidal basis function bounded between the surface and tropopause:

$$f_{\text{bc}1}(p) = -\sin\left(\pi \frac{p - p_{\text{TP}}}{p_s - p_{\text{TP}}}\right),$$

$$f_{\text{bc}2}(p) = -\sin\left(2\pi \frac{p - p_{\text{TP}}}{p_s - p_{\text{TP}}}\right), \quad (6)$$

The shallow-mode basis function is determined from the background ω field as explained later in section 3c(2). The three basis functions are drawn in Fig. 1.

The first baroclinic mode is often referred to as a deep convective mode and the second baroclinic mode with its sign flipped, or the negative second mode, is called a stratiform mode, based on the fact that the adiabatic heating structure associated with each vertical mode resembles the diabatic heating profile of the corresponding cloud type (Mapes 2000; Wu et al. 2000; Majda and Shefter 2001). In addition, the second baroclinic mode with low-level updraft (hereafter the positive second

mode) may be dynamically linked with congestus heating and is called a congestus mode (Khouider and Majda 2006; Kuang 2008b). The shallow mode is meant to account for heating confined to the lower troposphere that arises from shallow cumuli (Wu 2003; Waite and Khouider 2009). The three basis functions are expected as a whole to describe the large-scale dynamics within the context of a full spectrum of tropical convective clouds (Johnson et al. 1999).

The method for deriving the temporal evolution of Ω_{bc1} , Ω_{bc2} , and Ω_{shl} is described in section 3c(1), followed by section 3c(2), where the ancillary algorithm used to obtain ω_{bg0} and f_{shl} is outlined.

1) VERTICAL VELOCITY AND HORIZONTAL CONVERGENCE PROFILES

In this study, unlike an authentic approach based on the vertical spectral transformation of basic equations (e.g., Fulton and Schubert 1985), time series of the vertical velocity modes are diagnosed from the observed constraint on large-scale mean moisture and DSE convergences:

$$\begin{aligned}\bar{q} \frac{\partial \bar{\omega}}{\partial p} &= -\bar{q} \nabla \cdot \bar{\mathbf{v}} = -[\overline{\nabla \cdot q\mathbf{v}} - \overline{\nabla \cdot (q'\mathbf{v}')}] + [\overline{\mathbf{v} \cdot \nabla q} - \overline{\mathbf{v}' \cdot \nabla q'}], \\ \bar{s} \frac{\partial \bar{\omega}}{\partial p} &= -\bar{s} \nabla \cdot \bar{\mathbf{v}} = -[\overline{\nabla \cdot s\mathbf{v}} - \overline{\nabla \cdot (s'\mathbf{v}')}] + [\overline{\mathbf{v} \cdot \nabla s} - \overline{\mathbf{v}' \cdot \nabla s'}].\end{aligned}\quad (7)$$

The horizontal eddy terms above are negligibly small when the fluctuations in horizontal wind have no appreciable correlation with those in moisture and DSE and their horizontal gradient, an assumption valid for the spatial scales of present interest (~ 100 km) over tropical oceans (e.g., Yanai et al. 1973). Equation (7) is thus reduced to

$$\begin{aligned}\bar{q} \frac{\partial \bar{\omega}}{\partial p} &\approx -\overline{\nabla \cdot q\mathbf{v}} + \overline{\mathbf{v} \cdot \nabla q}, \\ \bar{s} \frac{\partial \bar{\omega}}{\partial p} &\approx -\overline{\nabla \cdot s\mathbf{v}} + \overline{\mathbf{v} \cdot \nabla s},\end{aligned}\quad (8)$$

It is noted that the vertical eddy transport of moisture and DSE is significant during active convection and explicitly included in the present formulation, as will be discussed in section 5c. For the moment, we focus on the vertical-mode decomposition of the large-scale mean field. Substituting the $\partial \bar{\omega} / \partial p$ term in (8) with the expanded series [(5)] and integrating vertically over the FT, one finds

$$\begin{aligned}\Omega_{bc1} \left\langle \bar{q} \frac{\partial f_{bc1}}{\partial p} \right\rangle_{FT} + \Omega_{bc2} \left\langle \bar{q} \frac{\partial f_{bc2}}{\partial p} \right\rangle_{FT} + \Omega_{shl} \left\langle \bar{q} \frac{\partial f_{shl}}{\partial p} \right\rangle_{FT} \\ = -\overline{(\nabla \cdot q\mathbf{v})}_{FT} + \overline{(\mathbf{v} \cdot \nabla q)}_{FT} - \left\langle \bar{q} \frac{\partial \bar{\omega}_{bg0}}{\partial p} \right\rangle_{FT}\end{aligned}\quad (9)$$

and

$$\begin{aligned}\Omega_{bc1} \left\langle \bar{s} \frac{\partial f_{bc1}}{\partial p} \right\rangle_{FT} + \Omega_{bc2} \left\langle \bar{s} \frac{\partial f_{bc2}}{\partial p} \right\rangle_{FT} + \Omega_{shl} \left\langle \bar{s} \frac{\partial f_{shl}}{\partial p} \right\rangle_{FT} \\ = -\overline{(\nabla \cdot s\mathbf{v})}_{FT} + \overline{(\mathbf{v} \cdot \nabla s)}_{FT} - \left\langle \bar{s} \frac{\partial \bar{\omega}_{bg0}}{\partial p} \right\rangle_{FT}.\end{aligned}\quad (10)$$

The convergence term on the right-hand side is as given by (3) and (4). At this point, $\bar{\omega}_{bg0}$ is also considered to be known. Another equation to solve is the boundary condition at cloud base,

$$\begin{aligned}\bar{\omega}_{bg0}(p_{CB}) + \Omega_{bc1} f_{bc1}(p_{CB}) + \Omega_{bc2} f_{bc2}(p_{CB}) \\ + \Omega_{shl} f_{shl}(p_{CB}) = \bar{\omega}(p_{CB}),\end{aligned}\quad (11)$$

whose right-hand side is determined by the continuity equation integrated over the SC:

$$\bar{\omega}(p_{CB}) = -\int_{p_s}^{p_{CB}} \overline{\nabla \cdot \mathbf{v}} dp = \overline{\nabla \cdot \mathbf{v}_{10} \Delta p_{SC}}.\quad (12)$$

As discussed earlier, horizontal wind is assumed to be vertically homogeneous within the SC.

We now have a closed system of three linear equations [(9)–(11)] that yield the three mode coefficients: Ω_{bc1} , Ω_{bc2} , and Ω_{shl} . The horizontal advection term in (9) and (10), however, has yet to be determined. This is resolved by an iterative procedure outlined as follows.

- (i) First, a slightly simplified version of (9)–(11) is solved with the horizontal advection term omitted. A solution is sought from one time step to the next until the whole time series of Ω_{bc1} , Ω_{bc2} , and Ω_{shl} are obtained. These solutions are derived individually for each 25-km-wide ring with increasing radii (0–25, 25–50, 50–75 km, etc.) that as a whole constitutes a circular large-scale domain that is then averaged over the entire domain as

$$\begin{aligned}\overline{[\dots]} &\equiv \frac{1}{\pi R^2} \int_0^R [\dots] 2\pi r dr \\ &\approx \frac{1}{R^2} \sum_{i=1}^{r_i=R} [\dots]_{i-1/2} (r_i^2 - r_{i-1}^2),\end{aligned}$$

where R ($=100$ km) is the large-scale-domain radius and r_i and r_{i-1} refer to the outer and inner radii of the $(i - 1/2)$ th ring. Subdividing the large-scale domain in this way facilitates computing horizontal advection.

- (ii) The vertical gradient of the p velocity is written in terms of the radial wind u as

$$\frac{\partial \omega(r, p)}{\partial p} = -\mathbf{V} \cdot \mathbf{v}(r, p) = -\frac{1}{r} \frac{\partial r u(r, p)}{\partial r}, \quad (13)$$

where r denotes the radial coordinate originating at the composite base point. Azimuthal wind does not appear in (13) because the azimuthal derivative term is integrated out by large-scale averaging. Equation (13) leads to the following formulation of radial wind:

$$\begin{aligned} u(r, p) &= -\frac{1}{r} \int_0^r \left[\frac{\partial \omega(r', p)}{\partial p} \right] r' dr' \\ &\approx -\frac{1}{2r} \sum_{i=1}^{r'_i=r} \left[\frac{\partial \omega}{\partial p} \right]_{i-1/2} (r_i^2 - r_{i-1}^2). \end{aligned} \quad (14)$$

The large-scale mean horizontal advection can be now computed as

$$\begin{aligned} \overline{\mathbf{v} \cdot \nabla q} &= u \frac{\partial q}{\partial r} \approx \frac{1}{R^2} \sum_{i=1}^{r_i=R} \left[u \frac{\delta q}{\delta r} \right]_{i-1/2} (r_i^2 - r_{i-1}^2), \\ \overline{\mathbf{v} \cdot \nabla s} &= u \frac{\partial s}{\partial r} \approx \frac{1}{R^2} \sum_{i=1}^{r_i=R} \left[u \frac{\delta s}{\delta r} \right]_{i-1/2} (r_i^2 - r_{i-1}^2), \end{aligned} \quad (15)$$

where u is given by (14) and $\delta/\delta r$ designates the upwind finite difference over r .

- (iii) The time series of Ω_{bc1} , Ω_{bc2} , and Ω_{shl} are updated with the complete forms of (9) and (10) and including the advection term in (15).
- (iv) The procedure from the first three steps is repeated until the solution converges. Convergence requires only six iterations, at most, since horizontal advection stays much smaller than horizontal convergence in the current applications. A brief discussion on the smallness of the horizontal advection is given in section 6.

2) BACKGROUND VERTICAL VELOCITY AND SHALLOW MODE

The three modes introduced above are augmented by the large-scale-mean time-invariant background field $\bar{\omega}_{bg0}$ to fully explain the observations. This constant background and the shallow mode, denoted collectively by the background shallow mode $\bar{\omega}_{bgs}$, are determined from the quiescent state devoid of active convection. The quiescent state is defined as the temporal average over the first and last 12-h sequences out of a ± 72 -h composite time series. During this stage, the precipitation stays constantly low at 0.2 mm h^{-1} (Masunaga 2013). The strategy for obtaining $\bar{\omega}_{bgs}$ parallels the procedure for finding the mode coefficients but uses a reduced version of (9)–(11):

$$\left\langle \frac{\partial \bar{\omega}_{bgs}}{\partial p} \right\rangle_{FT} = -\overline{\langle \mathbf{V} \cdot \mathbf{q}_0 \mathbf{v}_0 \rangle_{FT}}, \quad (16)$$

$$\left\langle \frac{\partial \bar{\omega}_{bgs}}{\partial p} \right\rangle_{FT} = -\overline{\langle \mathbf{V} \cdot \mathbf{s}_0 \mathbf{v}_0 \rangle_{FT}}, \quad (17)$$

and

$$\bar{\omega}_{bgs}(p_{CB}) = \bar{\omega}_0(p_{CB}), \quad (18)$$

where the two baroclinic modes and horizontal advection have been omitted since they are safely neglected in the absence of vigorous convection. The subscript 0 denotes the quiescent state.

A full vertical profile of $\bar{\omega}_{bgs}$ is derived with an additional requirement that $\bar{\omega}_{bgs}$ be as close as possible to the subsidence rate required to cancel radiative cooling $\bar{\omega}_{rad}$. The vertical structure of $\bar{\omega}_{rad}$ is computed directly from the observed DSE and radiative heating profiles:

$$\bar{\omega}_{rad} \frac{\partial \bar{s}_0}{\partial p} = \bar{Q}_{R,0}. \quad (19)$$

The background shallow mode is determined by minimizing

$$\sum_{p=p_s}^{p_{TP}} [\bar{\omega}_{bgs}(p) - \bar{\omega}_{rad}(p)]^2 \quad (20)$$

under the constraints of (16)–(18). This procedure is performed by following the Lagrangian multiplier method, which provides 16 equations (13 levels + 3 constraints) to find 16 unknowns that include $\bar{\omega}_{bgs}$ given at all pressure levels.

Figure 2 shows that $\bar{\omega}_{bgs}$ is found to be bimodal, consisting of a primary peak around 400–500 hPa and a weaker one at cloud base. The upper peak is consistent with midtropospheric large-scale ascent typical of tropical climate (e.g., Nitta 1972; Yanai et al. 1973; Thompson et al. 1979; Houze 1982; Lin and Johnson 1996), while the lower peak is presumably associated with shallow cumuli prevailing across tropical oceans as well (Yanai et al. 1976). In the current formulation, the upper peak is considered to be $\bar{\omega}_{bg0}$ and the lower one is thought of as the shallow mode. The shallow mode is detached from the constant background so it is allowed to vary with time. The shallow updraft $\bar{\omega}_{shl}$ is separated from $\bar{\omega}_{bg0}$ in a simple manner such that

$$\bar{\omega}_{shl}(p) = \begin{cases} 0 & \text{for } p < 850 \text{ hPa} \\ \bar{\omega}_{bgs}(p) - \bar{\omega}_{rad}(p) & \text{for } p \geq 850 \text{ hPa} \end{cases}$$

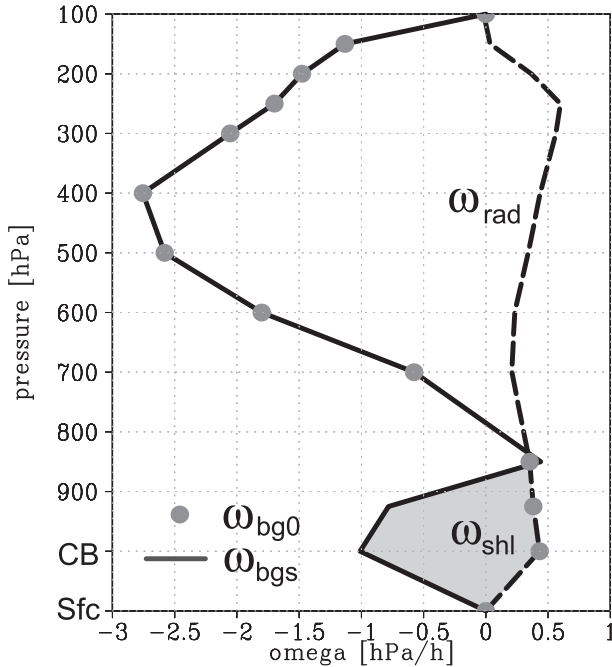


FIG. 2. Subsidence rate balanced against radiative cooling (dashed), and background shallow mode p velocity (solid), as well as its breakdown into its time-invariant component (filled circle), and shallow mode (shaded).

and

$$\bar{\omega}_{bg0}(p) = \begin{cases} \bar{\omega}_{bgs}(p) & \text{for } p < 850 \text{ hPa} \\ \bar{\omega}_{rad}(p) & \text{for } p \geq 850 \text{ hPa} \end{cases}$$

(see Fig. 2). Note that $\bar{\omega}_{bg0} + \bar{\omega}_{shl} = \bar{\omega}_{bgs}$ for all pressure levels. The shallow-mode basis function is defined by normalizing $\bar{\omega}_{shl}$ as

$$f_{shl}(p) = \frac{\bar{\omega}_{shl}(p)}{\bar{\omega}_{shl}(p_{CB})}. \quad (21)$$

The shallow and background modes as defined here are not orthogonal to the two baroclinic modes introduced earlier. The lack of orthogonality does not violate mathematical self-consistency in the current method, which only involves the observationally constrained algebraic equations without invoking any spectral transformation. By design, the background shallow mode explains the whole budget residual unaccounted for by the first two baroclinic modes and, hence, in theory absorbs the contributions from all of the higher-order modes. It is also noted that the minimization operation [(20)] should not be confused as the solution is obtained through a least squares fit to the budget constraint and thus is exact only to that extent.

Rather, (20) represents the assumption that the background sounding is as close as possible to the radiatively driven subsidence under the condition that the budget equations [see (16)–(18)] be satisfied exactly.

4. Results

In this section, the evolution of the MSE budget parameters is presented and examined within the context of vertical-mode decomposition.

a. MSE budget and GMS

Vertically integrating and horizontally averaging (2) leads to an equation for quantifying the large-scale mean moisture convergence:

$$-\langle \nabla \cdot q \mathbf{v} \rangle = \frac{\partial}{\partial t} \langle q \rangle - \bar{E} + \bar{P}_s. \quad (22)$$

The right-hand side contains known observables only [see discussion in section 3c(1)] and is used as a diagnostic measure of moisture convergence integrated over the whole troposphere. Similarly, the MSE conservation equation serves as a formula for estimating MSE convergence:

$$-\langle \nabla \cdot h \mathbf{v} \rangle = \frac{\partial}{\partial t} \langle h \rangle - L\bar{E} - S - \langle Q_R \rangle, \quad (23)$$

where $h \equiv s + Lq$ is MSE.

Figure 3 delineates the composite time series of moisture and MSE convergences estimated with (22) and (23). The time of the precipitation occurrence detected by the TRMM PR defines time 0 in the composite time series. Moisture convergence is enhanced during periods of active convection, largely counteracted by precipitation with minimal contributions from surface evaporation and moisture storage (Fig. 3a). It is noted that the magnitude of moisture convergence depends on the intensity of the associated convection and would weaken to a level only slightly greater than local evaporation when composited with respect to isolated cumuli (Masunaga 2013). MSE convergence (solid curve in Fig. 3b) begins slightly negative and gradually approaches zero before abruptly dropping at the time of peak convection and then slowly increasing toward zero again. The weak MSE divergence at the initial (or background) stage is balanced by the surface latent heat supply (dashed) and the radiative cooling (dotted-dashed). Sensible heat flux (dotted) is negligible throughout. The MSE storage term (shaded) exhibits a systematic increase over time with the exception of a sudden drop in the middle, closely paralleling the temporal evolution of the MSE divergence.

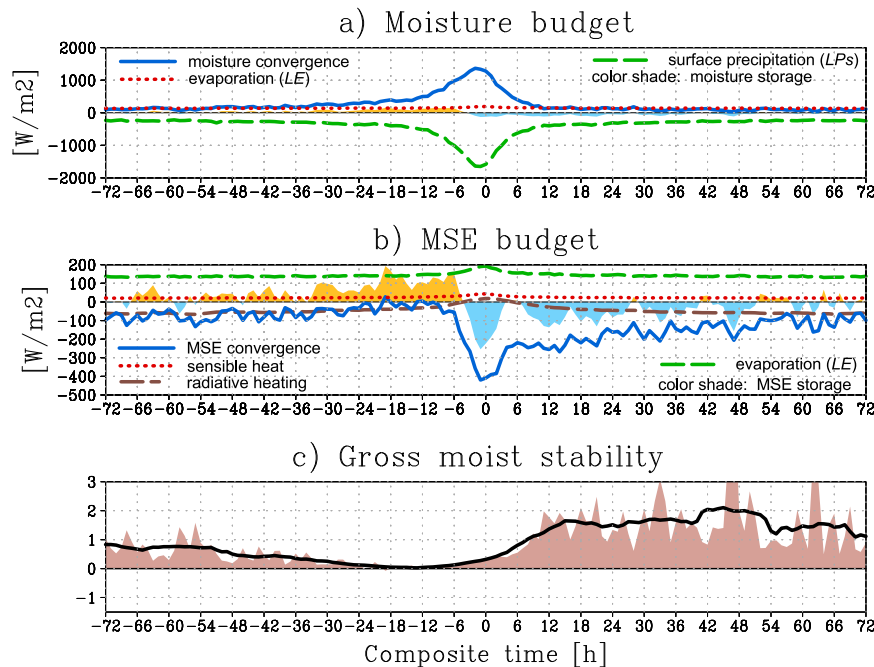


FIG. 3. Composite time series of moisture and MSE budget parameters. (a) Moisture convergence (blue solid), surface precipitation (green dashed), evaporation (red dotted), and moisture storage (shaded), all scaled by L into the energy unit ($W m^{-2}$). (b) MSE convergence (blue solid), evaporation (green dashed), sensible heat (red dotted), radiative heating (brown dotted-dashed), and MSE storage (shaded; $W m^{-2}$). (c) Raw (shaded) and smoothed (solid) normalized GMS (no units). A ± 6 -h running mean is applied to the smoothing of GMS.

These estimates of moisture and MSE convergences make it possible to explicitly evaluate a slightly modified version of the “normalized GMS” proposed by Raymond et al. (2007):

$$GMS \equiv -\frac{\langle \mathbf{V} \cdot h\nabla \rangle}{L \langle \mathbf{V} \cdot q\nabla \rangle}. \quad (24)$$

The time series of GMS (Fig. 3c) suffers a statistical fluctuation that arises when the denominator (moisture convergence) diminishes to within the noise level around zero. With the noises smoothed out by ± 6 -h running mean, GMS is found to gradually decrease from about 1 and nearly vanishes at -24 h. After remaining close to zero until -6 h, GMS slowly climbs back to a level on the order of unity but somewhat higher than its initial value. Typical values of the normalized GMS in the literature range between 0.1 and 0.6 (Raymond et al. 2009; Sugiyama 2009a), roughly comparable to the present estimate when averaged over time. Figure 3 suggests, however, that GMS should have a systematic temporal evolution associated with convective growth and decay. Physical processes relevant to the GMS variability and underlying dynamics will be explored in section 5.

b. Vertical motion and mode decomposition

Figure 4 shows the vertical structure of large-scale mean p velocity [the sum of all modes constructed through (5)] and horizontal convergence obtained as a by-product. A strong updraft sharply develops within 12 h of time 0 and gives rise to a midtropospheric maximum around 500 hPa before quickly dissipating. The structural evolution of horizontal convergence is characterized by a deepening of the lower-tropospheric convergence prior to convection, followed by an abrupt SC, divergence likely due to convective downdraft. A coupling of lower-tropospheric convergence and upper-tropospheric divergence is evident at the peak time of convection, a feature known to accompany organized convective systems (Mapes and Houze 1995).

The breakdown into individual ω -mode coefficients is presented in Fig. 5a. The first baroclinic mode rapidly grows to a prominent peak and then dies out quickly, closely in line with the moisture convergence and precipitation (Fig. 3a). The first mode largely dominates the other modes in amplitude (note that Ω_{bc1} is rescaled as labeled along the right axis) and is almost solely responsible for establishing the midtropospheric updraft maximum seen in Fig. 4a. The second baroclinic mode

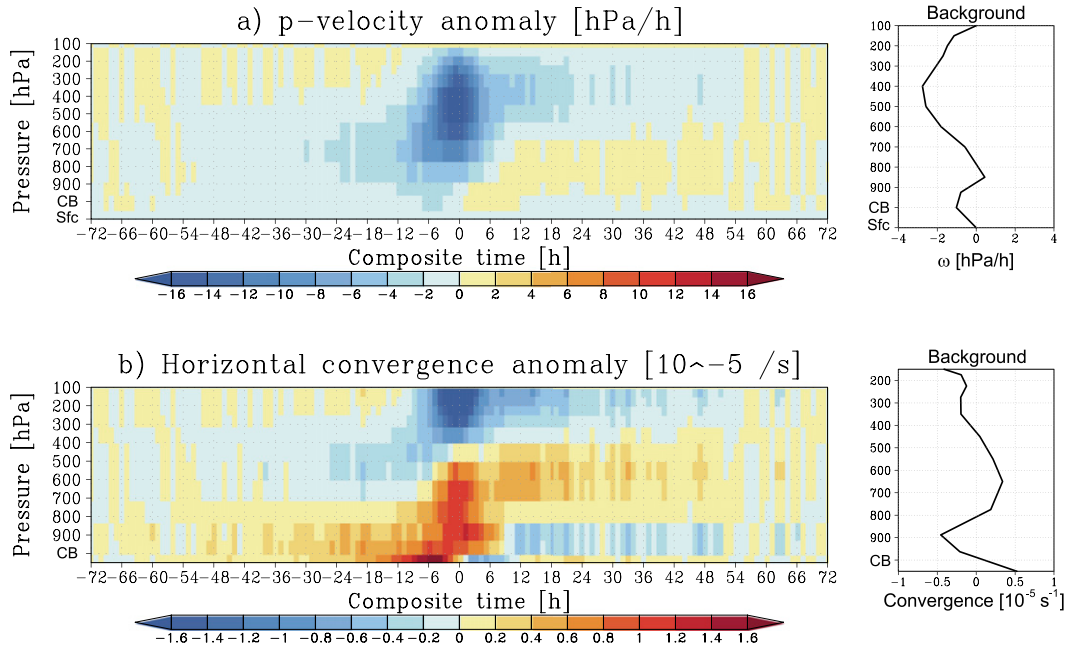


FIG. 4. (left) Composite time series of (a) the large-scale mean vertical velocity anomaly and (b) the horizontal convergence anomaly. The anomaly is defined against (right) the background (the first and last 12-h sequences averaged together).

initially emerges as the positive mode and gradually evolves until around -6 h, when Ω_{bc2} suddenly becomes negative. The negative second mode then slowly declines and eventually disappears. The shallow mode stays nearly constant aside from a “dip” shortly after the time of peak convection, when Ω_{shl} momentarily hits zero.

The evolution of precipitating-cloud occurrence is presented in Fig. 5b for comparison with the vertical-mode coefficients. Each of the cloud types shown here (i.e., shallow, convective, and stratiform) is derived from the precipitation-type flag from the *CloudSat* 2C-PRECIP-COLUMN product. Congestus clouds are likely represented by the shallow category but may be partially

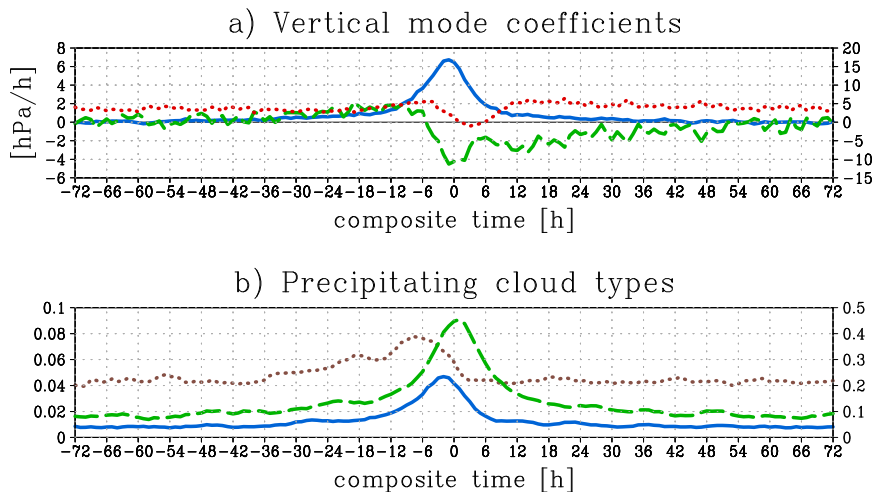


FIG. 5. Composite time series of the vertical modes and precipitating cloud occurrences. (a) Vertical velocity mode coefficients for the first baroclinic mode (blue solid; labeled on the right axis), second baroclinic mode (green dashed), and shallow mode (red dotted). (b) *CloudSat* precipitation occurrence for the three cloud types of convective (blue solid), stratiform (green dashed; labeled on the right axis), and shallow/congestus (brown dotted).

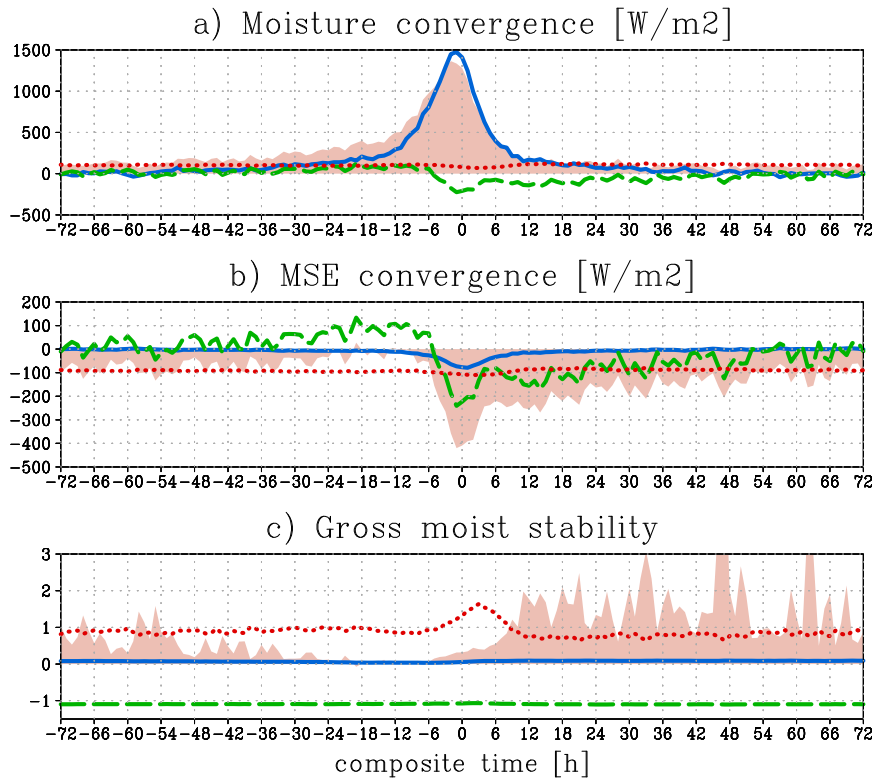


FIG. 6. Composite time series of (a) moisture convergence, (b) MSE convergence, and (c) GMS, each broken down into the first baroclinic mode (blue solid), second baroclinic mode (green dashed), and background shallow mode (red dotted). The total is shaded.

classified as convective when the cloud top develops relatively deeply. The population of shallow/congestus clouds gradually increases over time until they give way to stratiform clouds around -6 h. This behavior appears to support the expectation that the first and second halves of the second baroclinic mode are associated with congestus and stratiform clouds, respectively. Convective clouds, on the other hand, bear similarity to the first baroclinic mode. The convective curve reaches a peak just 1–2 h before time 0 in accordance with the first mode peak, followed a few hours later by the stratiform peak. Convective clouds have smaller areal coverage than stratiform clouds by almost an order of magnitude, although convective clouds are known to predominate in rainfall, and thus in condensational heating, once vigorous deep convective cores develop.

5. Mechanics of GMS variability

a. Mode decomposition of GMS and a mechanism of tropical convection

Once the vertical mode coefficients are obtained, moisture convergence can be similarly decomposed into

individual modes as expanded in (9). Figure 6a shows that the first baroclinic mode alone nearly describes the moisture convergence as one might expect from its predominance over other modes (Fig. 5a). In contrast, the evolution of MSE convergence arises from a more even competition among the three modes (Fig. 6b). A weak MSE divergence in the background state is more strongly counteracted by a growing MSE convergence brought on by the positive second mode (congestus mode) as time proceeds. The second mode then becomes sufficiently strong to totally cancel out the background shallow mode, resulting in zero MSE convergence prior to the peak convection, as observed in Fig. 3b. The positive second mode suddenly switches to the negative mode at -6 h, which introduces a sudden onset of MSE divergence that now enhances (rather than competing against) the diverging background. The first mode also momentarily strengthens the MSE divergence but remains minimal through the rest of the period. The MSE divergence gradually weakens as the second mode tapers off after the convection ceases.

The contrast among the different patterns of behavior specific to each mode is best illustrated in GMS (Fig. 6c). Different GMS modes are defined here simply as the

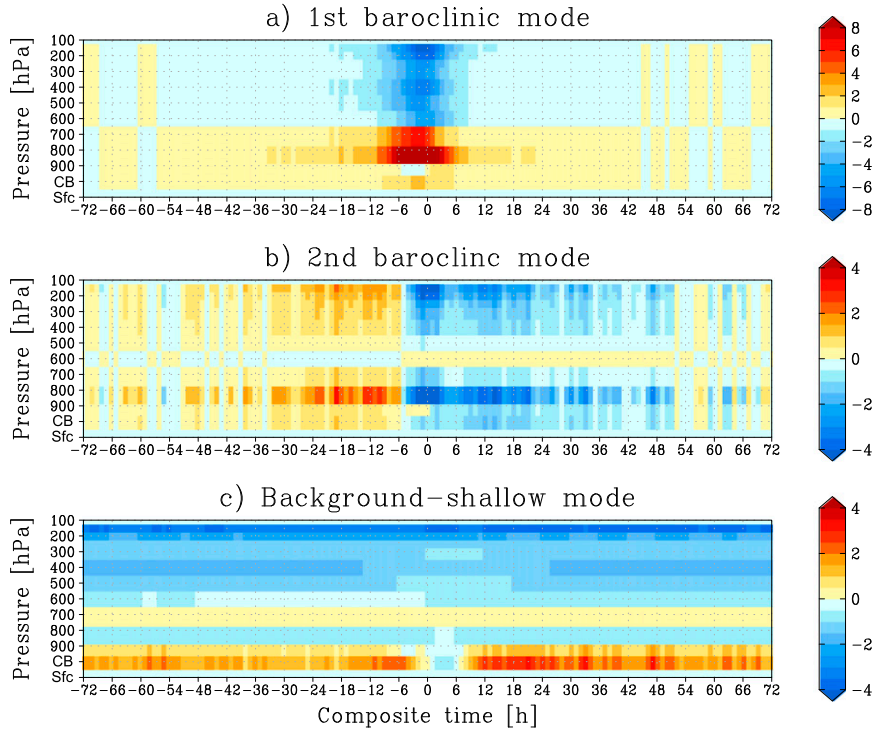


FIG. 7. Composite time series of large-scale mean vertical MSE advection (K day^{-1}) for the (a) first baroclinic mode, (b) second baroclinic mode, and (c) background shallow mode.

ratio of the MSE and moisture convergences that are individually computed, and hence the decomposed modes do not sum to the original GMS. GMS stays positive for the background shallow mode, while the second baroclinic mode is consistently negative in GMS. The first baroclinic mode virtually vanishes throughout. The constant nature of GMS for the two baroclinic modes arises from a near cancellation of time-dependent mode coefficients between the numerator and denominator in (24).

Reasons why the different GMS modes are diverse in sign and magnitude can be understood as follows. MSE convergence is mathematically equivalent to the vertically integrated vertical advection of MSE:

$$\left\langle \bar{h} \frac{\partial \bar{\omega}}{\partial p} \right\rangle = - \left\langle \bar{\omega} \frac{\partial \bar{h}}{\partial p} \right\rangle. \quad (25)$$

In the mean tropical sounding, MSE decreases with height, reaching a midtropospheric minimum and then increases with height aloft; that is, $\partial \bar{h} / \partial p$ is positive in the lower troposphere and negative in the upper troposphere. Given this feature common to all vertical modes, the nature of MSE convergence depends on the shape of the $\bar{\omega}$ profile in (25). The first baroclinic mode, for which $\bar{\omega} < 0$ at all pressure levels, yields a vertical MSE

advection that changes sign from positive to negative with large-scale upward motion through the middle troposphere (Fig. 7a). Vertical MSE advection, although very large at individual levels, is canceled out to a large extent when integrated vertically and therefore the contribution of the first mode to MSE convergence is unexpectedly small (Fig. 6b) despite its dominant share in large-scale dynamics (Fig. 5a). Recalling as well that the first mode gives rise to robust moisture convergence (Fig. 6a), one finds that the first mode has the effect of strongly reducing GMS.

For the second baroclinic mode, $\bar{\omega}$ has opposite signs between the lower and upper halves of the troposphere. It follows that vertical MSE gradient and $\bar{\omega}$ each change sign at the same height and would in tandem make vertical MSE advection entirely positive or negative throughout the troposphere. Figure 7b confirms this simple deduction, with the exception of a thin layer at 600 hPa where the MSE minimum and the second-mode node have a slight difference in altitude. The positive second mode results in MSE import and the negative mode leads to MSE export at almost all heights, explaining the abrupt change in MSE convergence at -6 h when the second mode changes sign (Fig. 6b). A similar transition occurs simultaneously in moisture convergence (Fig. 6a), so GMS stays negative at all times for

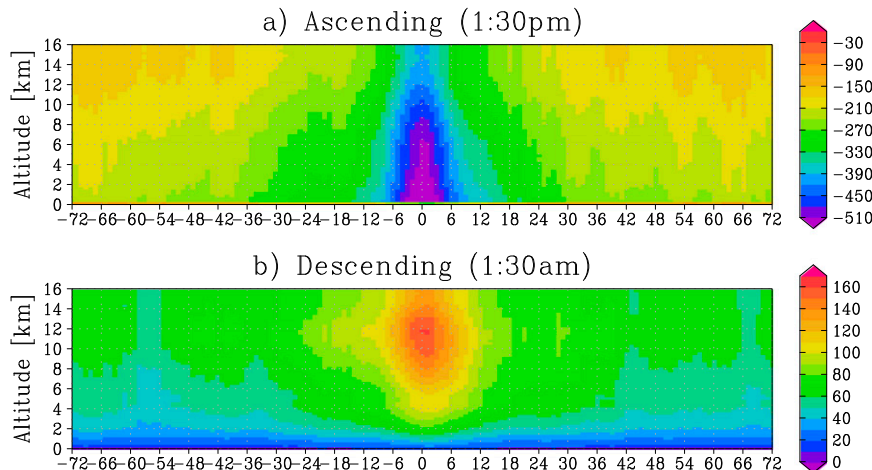


FIG. 8. Composite time series of the vertical profile of cloud radiative effect (W m^{-2}) constructed with (a) ascending or afternoon (1330 LT) paths and (b) descending or midnight (0130 LT) paths.

the second mode. This is the origin of the unique importance of the second baroclinic mode in the mechanism of tropical convection, as discussed later.

The upper-troposphere-peaked $\bar{\omega}_{\text{bg0}}$ profile (Fig. 2) makes MSE divergent (Fig. 7c), although MSE is imported to a lesser extent by the lower-troposphere-peaked $\bar{\omega}_{\text{shl}}$. These two competing processes explain a weak MSE divergence in the background shallow mode.

A modest moisture import is persistently driven by the shallow mode except during a short period immediately after the convective peak. The shallow mode is temporarily shut off during this period, which may likely be ascribed to a downdraft of dry, cold air. The transient cutoff in moisture convergence is responsible for the spike in the background shallow-mode GMS (Fig. 6c).

The findings thus far may be summarized into a working hypothesis for a mechanism of tropical convection. GMS slowly diminishes from a positive value on the order of unity to zero prior to convection, primarily due to a weakening of MSE divergence. The reduction of GMS is ultimately attributable to the growth of the congestus mode, which in theory has a negative GMS if acting alone. GMS, however, stays tightly bound to zero. This may be explained by the fact that a reduction of GMS allows the convection to deepen and helps the first baroclinic mode, having zero GMS, to dominate. In other words, a deep updraft acts against the onset of MSE convergence because it activates an upper-tropospheric MSE export that closely cancels out the lower-tropospheric MSE import. Nevertheless, GMS staying near zero finally gives rise to a vigorous convective burst accompanying a drastic amplification of the first mode. The convective burst, however, is not

sustained for long as it is followed by a rapid buildup of MSE divergence coinciding with a transition of the congestus mode into the stratiform mode. The restoration of MSE divergence brings GMS back to a positive value and puts an end to the period of enhanced large-scale updraft driven by active convection.

There remain two MSE budget terms (i.e., radiative heating and convective eddy transport) that have yet to be examined. They are each investigated in the remainder of this section.

b. Effects of radiative heating on the MSE budget

The composite diagrams presented so far are constructed from all satellite orbits with no distinction in the local time of observation. The ascending and descending orbital swaths are individually analyzed in this section so that afternoon (1330 LT) and midnight (0130 LT) observations are separated to depict the diurnal contrast in radiative heating. The afternoon observations of shortwave radiation qualitatively reflect daytime-mean climatology but exaggerate its magnitude as noted in section 2. Note that the entire calculations including $\bar{\omega}_{\text{rad}}$ in (19) are redone individually with the morning or afternoon path.

Figure 8 shows the vertical profile of the cloud radiative effect (CRE) defined as

$$\text{CRE} = (F_{\text{clr}}^{\uparrow} - F_{\text{clr}}^{\downarrow}) - (F_{\text{all}}^{\uparrow} - F_{\text{all}}^{\downarrow}),$$

where F_{clr} and F_{all} are the net (shortwave plus longwave) radiative fluxes for clear and all skies, respectively, and arrows indicate upwelling (\uparrow) and downwelling (\downarrow) fluxes. Note that the *CloudSat* radiative flux product is derived from broadband radiative transfer calculations

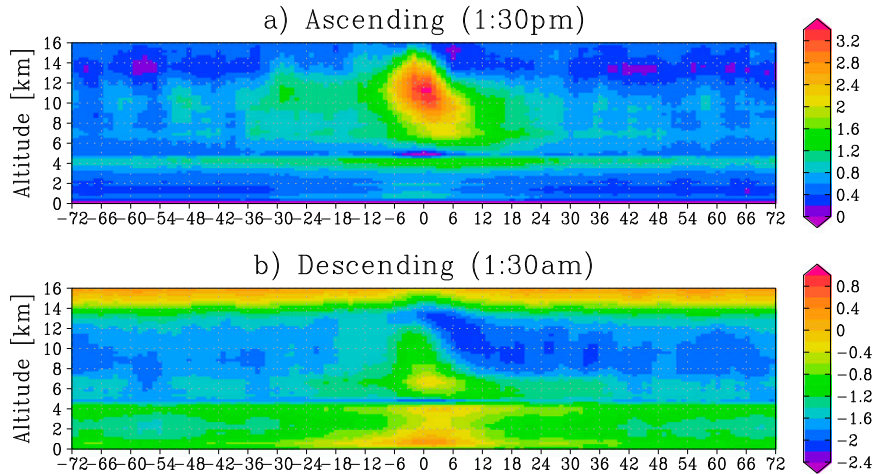


FIG. 9. As Fig. 8, but for the radiative heating rate (K day^{-1}).

applied to the observed cloud properties, making a synthetic “clear sky” estimate readily available by eliminating clouds internally in the radiative transfer model (Henderson et al. 2013). A sharp minimum occurs at the time of convection and falls deeper as altitude decreases in the afternoon CRE (Fig. 8a). This striking feature arises from the cloud shielding incoming shortwave radiation as well as an elevated greenhouse effect due to cirrus and cirrostratus clouds detrained from penetrating convection. The longwave effect is solely observed in CRE at midnight (Fig. 8b), where a broad upper-tropospheric maximum develops during active convection as expected.

The vertical distribution of the net radiative heating rate Q_R is plotted in Fig. 9. In the afternoon, radiative heating is marked by elevated shortwave cloud absorption during active convection in the upper troposphere (Fig. 9a). Longwave cooling at the tops of melting-layer clouds, frequently observed over tropical oceans (Mapes and Zuidema 1996; Yasunaga et al. 2006), are likely responsible for the sharp discontinuity at a height of 4–5 km. The midnight composite (Fig. 9b) shows that the greenhouse effect is mildly modulated by convective activity in the lower and midtroposphere while at upper levels, in contrast, a cloud-top cooling develops immediately after time 0.

This temporal evolution remains visible but is not as prominent in the total tropospheric cooling ($\langle Q_R \rangle$) (Fig. 10), since the upper-tropospheric contribution is diluted to some extent by the density-weighted vertical integral. More evident is the diurnal contrast that arises between the afternoon heating slightly below 100 W m^{-2} (Fig. 10a) and the midnight cooling at -200 W m^{-2} (Fig. 10b). A caveat is that any day-long temporal sequence in reality must involve a diurnal cycle superimposed while the

composite time series in this work by design lacks it. The current compositing technique is unrealistic in this regard and care must be taken not to overinterpret the results.

Another notable feature of Fig. 10 is that MSE convergence (dotted) no longer vanishes but stays negative (afternoon) or positive (midnight) prior to active convection. It is instead the sum of MSE and radiative heating (solid) that consistently approaches zero in all cases. The working hypothesis argued in section 5a remains valid but must be revised to note that MSE convergence is augmented by radiative heating. Accordingly, GMS is modified with a radiative cooling rate added to the numerator,

$$\text{GMS}(\text{updated}) = -\frac{\overline{\langle \mathbf{V} \cdot h\mathbf{v} \rangle} - \overline{\langle Q_R \rangle}}{L \overline{\langle \mathbf{V} \cdot q\mathbf{v} \rangle}}, \quad (26)$$

which is conceptually equivalent to the “effective GMS” introduced by Su and Neelin (2002) and Bretherton and Sobel (2002). Figure 11 shows two versions of GMS (smoothed over time for visual clarity) that are obtained with or without radiative heating included in the numerator. The time axis ends at 24 h because the sample-size reduction from separating day and night increases the statistical noise in the denominator of GMS to an intolerable level for $t > 24$ h. The large dispersion between the afternoon and midnight composites inherent in the original definition of GMS given by (24) (Fig. 11a) is substantially reduced when the numerator is updated to include radiative heating via (26) (Fig. 11b). GMS is confirmed to offer a more universal reference to the mechanism of tropical convection when radiative effects are explicitly taken into account.

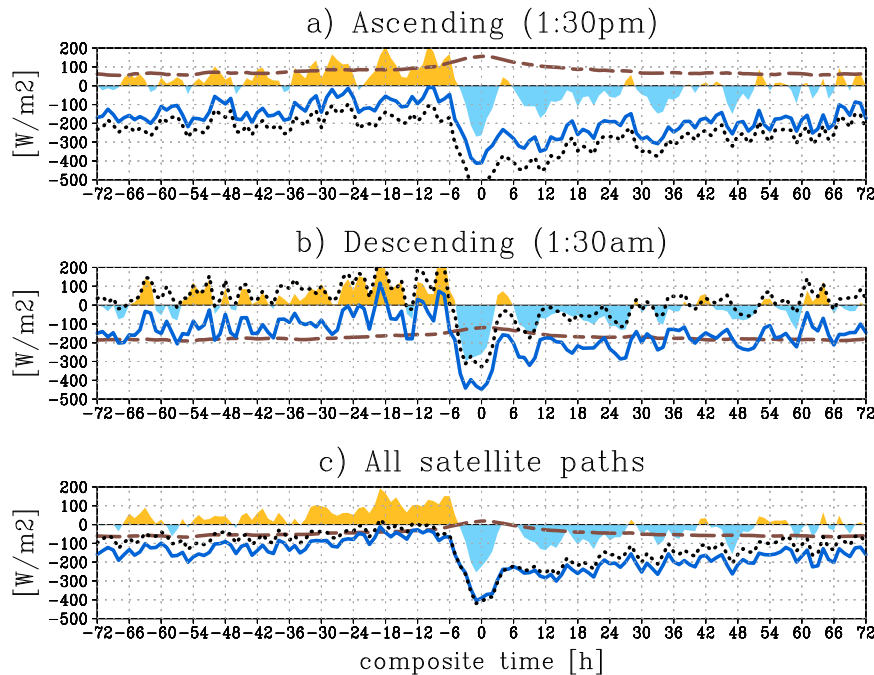


FIG. 10. Vertically integrated MSE convergence (black dotted), radiative heating (brown dotted-dashed), their sum (blue solid), and MSE storage (color shaded) for (a) ascending or afternoon (1330 LT) paths only, (b) descending or midnight (0130 LT) paths only, and (c) all satellite paths.

c. Vertical eddy transport of MSE

It has been seen that the combination of vertically integrated MSE convergence and radiative heating nearly vanishes preceding the growth of convection. This may be physically interpreted to mean that a coordinated growth of convection and large-scale updraft

is promoted when the diabatic heating source reaches a level sufficient for the ascent to work against large-scale adiabatic cooling. This argument, however, is incomplete in that only the vertically integrated MSE budget has been examined so far. An additional mechanism is needed to internally transport the latent heating

All satellite paths (solid), ascending only (dashed), and descending only (dotted)

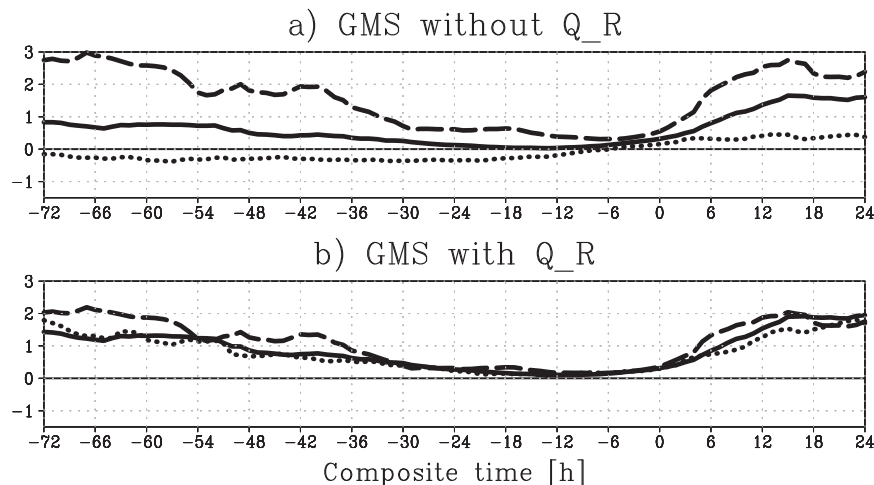


FIG. 11. Composite time series of GMS smoothed temporally by a ± 6 -h running mean. (a) Original definition from (24) and (b) updated definition in (26) with radiative heating included in the numerator. Hours beyond +24h are omitted.

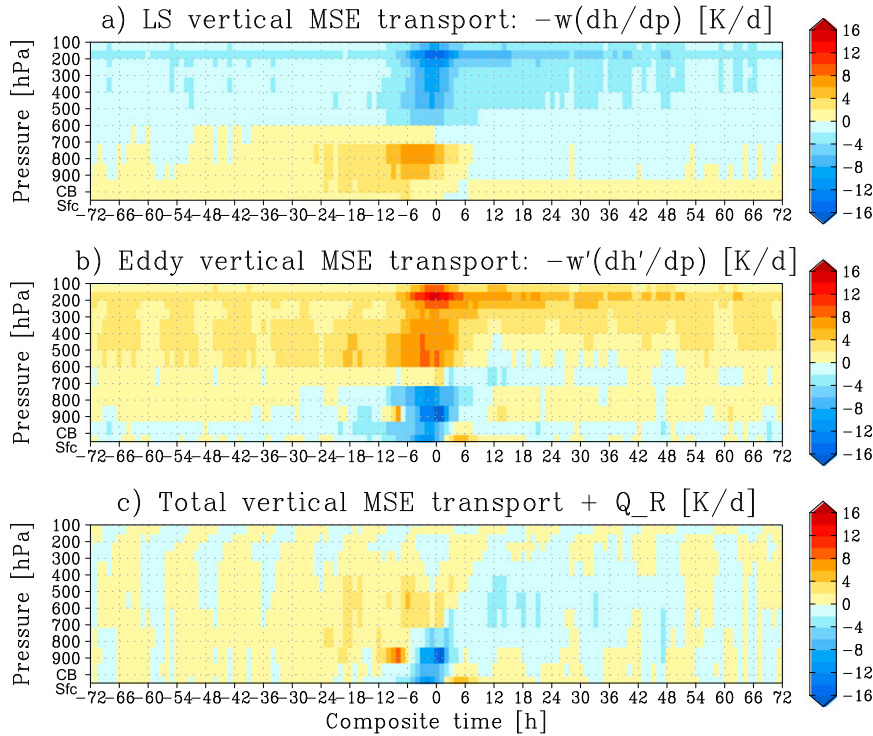


FIG. 12. Composite time series of (a) large-scale mean vertical MSE advection (K day^{-1}), (b) vertical eddy MSE transport (K day^{-1}), and (c) total MSE transport plus Q_R (K day^{-1}).

from low-level moisture to the upper troposphere, where an upward-increasing MSE hampers vertical motion from occurring spontaneously. The solution to this problem has been known since the pioneering work of Riehl and Malkus (1958), who found that towering convective clouds are a key ingredient in the vertical redistribution of MSE. The thermodynamic impact of condensational heating was later formulated in terms of eddy energetics by Manabe and Smagorinsky (1967), Nitta (1970) and in subsequent energy budget studies (e.g., Yanai et al. 1973). This section is devoted to a brief investigation of vertical eddy transport as a bulk measure of the convective effects on the MSE budget, aimed at confirming that the current analysis is in line with the literature.

Averaging (1) horizontally, one finds the large-scale mean MSE budget equation

$$\frac{\partial \bar{h}}{\partial t} + \bar{\mathbf{v}} \cdot \nabla \bar{h} + \bar{\omega} \frac{\partial \bar{h}}{\partial p} = \bar{Q}_R - \overline{\omega' \frac{\partial h'}{\partial p}}, \quad (27)$$

where the last term refers to the vertical eddy transport of MSE. The eddy advection term $\overline{\omega' \partial h' / \partial p}$ is interchangeable with the flux-form expression of the vertical eddy transport $\partial \bar{h}' \omega' / \partial p$ when horizontal eddy flux is negligible. All terms in (27) except the last one are known at every height from the present analysis so far,

so this equation can be used to evaluate the vertical profile of eddy MSE transport as a residual of the other terms.

A striking contrast is evident between large-scale mean vertical MSE advection (Fig. 12a) and its eddy counterpart (Fig. 12b). Large-scale mean vertical advection, or the third term on the left-hand side of (27), is positive in the lower troposphere and negative in the upper troposphere, primarily in response to the first baroclinic mode (Fig. 7a). The vertical eddy advection of MSE, on the other hand, consists of an upper-tropospheric positive and a lower-level negative component. The positive eddy advection aloft is presumed to originate from convective plumes through which high-MSE air in the subcloud layer is lifted moist adiabatically to the level where it is detrained. At the same time, a mesoscale downdraft in a mature convective system draws down midtropospheric low-MSE air and is speculated to account for the negative eddy advection in the lower troposphere. The competing effects of large-scale dynamics and convective eddies, with the radiative heating profile taken into account, largely cancel each other but leave behind a faint residual (Fig. 12c). Equation (27) indicates that the storage and horizontal advection terms make up this residual, with the former dominating the latter since MSE is horizontally homogeneous

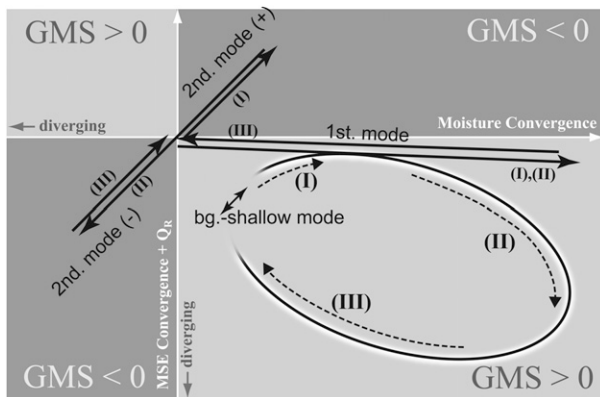


FIG. 13. Schematic summary. Trajectories are projected onto the plane of moisture convergence (abscissa) and MSE convergence plus radiative heating (ordinate).

over the spatial scale of interest. A temporary lower-tropospheric negative around time 0 in Fig. 12c suggests that the drying due to convective downdraft overcompensates the moistening by large-scale ascent at the convective peak. This possibly has the effect of hindering the convective system from intensifying further.

6. Conclusions and discussion

Observations from multiple satellite platforms are coordinated to perform a composite analysis of the temporal variability associated with convective development within the context of the MSE budget. The analysis is designed to yield a statistically continuous time series of the atmospheric state prior and subsequent to the occurrence of convection by compositing pairs of satellite measurements with respect to the observational lag or lead time between them. Observational thermodynamic constraints are then exploited to evaluate large-scale vertical motion through vertical mode decomposition.

A schematic summary of the results is presented in Fig. 13, where the temporal variability in the MSE budget is illustrated in terms of moisture convergence (abscissa) and MSE convergence plus radiative heating (ordinate). GMS is defined on this plane as the inclination of the vector pointed from the origin to a given point, with its sign indicated in each quadrant of the figure. GMS is therefore close to zero near the abscissa and increases in absolute value moving toward the ordinate.

The first baroclinic mode spans a long distance bound to the abscissa, while the second mode stays on a short slanted path, which moves back and forth between the quadrants of negative GMS. The background shallow mode barely deviates from the background state having

modest values of moisture convergence and MSE divergence. The trajectory of the observed temporal evolution follows an oval-like path, as schematically drawn in Fig. 13, and can be explained in terms of three distinct stages.

- *Stage I* ($t < -6$ h)—The background MSE divergence is gradually offset toward zero by the MSE convergence brought about by the positive second baroclinic mode (congestus mode). The congestus mode consists of modest lower-tropospheric ascent associated with congestus clouds and upper-level subsidence, which together import both moisture and MSE. Recalling that the background vertical motion consists of a weak upper-tropospheric updraft, one could attribute the upper-level subsidence in the second mode to a gradual weakening of the background ascent during periods devoid of vigorous disturbances. GMS is driven close to zero, a critical line for an unstable growth of moist convection to occur. The first baroclinic mode and deep convection begin to intensify.
- *Stage II* ($-6 < t < 0$ h)—The growth of vigorous large-scale updrafts accelerates sharply in concert with a burst of deep convection. This involves the development of the first baroclinic mode, in which a low-level MSE import is now totally (or even excessively) compensated by an upper-level MSE export. A negative GMS thus does not occur but GMS remains zero during this stage. At the same time, the positive second mode switches to the negative mode (stratiform mode), presumably concurrent with the onset of a lower-tropospheric downdraft characteristic of the development of stratiform rain in mature convective systems. The onset of the stratiform mode introduces an abrupt rise in MSE divergence and now makes the thermodynamic environment less favorable for convection development.
- *Stage III* ($t > 0$ h)—The first mode and deep convection rapidly dissipate. The stratiform mode also weakens but more slowly. At this stage, MSE is diverging while moisture is converging once the momentary low-level downdraft ceases, which together leads to a positive GMS. GMS increases away from zero and is restored to beyond the initial level as the background shallow mode alone is being left behind.

These three stages are reminiscent of a recent school of thought for convectively coupled equatorial waves where the first and second baroclinic modes alternate with each other in line with the progression where congestus clouds gradually grow deeper and finally give way to stratiform clouds (e.g., Khouider and Majda 2006; Peters and Bretherton 2006; Kuang 2008a,b).

Similar mechanics are shown to be at work within a general meteorological context beyond wave dynamics. Among the family of tropical waves ranging over a wide spectrum of frequencies, the 2-day waves are of particular interest because they are similar in time scale to the variability found in this study. The 2-day wave dynamics is known to be explained in terms of the first two or three baroclinic modes developing one after another (Haertel and Kiladis 2004; Haertel et al. 2008) in a manner parallel with the findings of this work. It is unclear whether the 2-day waves have a dominant influence on the fundamental nature of tropical convection or, conversely, whether some intrinsic time scale inherent in the convective effects on large-scale dynamics controls the scale selection in favor of the 2-day mode, or possibly the resemblance may be little more than coincidence.

The destabilizing mechanism is explained primarily by the MSE import intrinsic to the congestus mode in the present picture, resembling the “discharge–recharge” scenario discussed by Peters and Bretherton (2006). This involves large-scale dynamics only and does not necessitate an FT moistening through congestus clouds or “preconditioning” (e.g., Waite and Khouider 2010; Hohenegger and Stevens 2013).

One of the intriguing findings above is that GMS is anchored tightly to zero without going negative during the convective intensification. A negative GMS, with MSE and moisture both converging, is not observed, as theorized by Raymond et al. (2009) and simulated by Sessions et al. (2010), but instead zero GMS appears to be sufficient to drive an accelerating growth of large-scale updrafts. A key element that keeps GMS from becoming negative is the quick development of the first mode that efficiently exports high MSE in the upper troposphere. A dry-gets-drier case of negative GMS is also worth attention (Bretherton et al. 2005; Sessions et al. 2010) but is outside the scope of the present analysis. Our compositing technique is built around the time of convection and, by design, excludes a prolonged absence of precipitation.

GMS provides a more reliable metric when radiative heating is included in its definition [“effective GMS”; see (26)]. This conclusion is drawn from the fact that MSE convergence plus radiative heating rate rather than MSE convergence alone follows a consistent evolutionary track in comparisons between the afternoon and midnight composite diagrams. Nocturnal convection accompanies a larger (even a positive) MSE convergence than does afternoon convection so as to work against a greater radiative cooling due to the absence of shortwave absorption. This supports the arguments of Randall et al. (1991), who found that a diurnal cycle in large-scale vertical motion over the ocean arises in their

model because the cloud absorption of solar radiation somewhat stabilizes the upper troposphere during the daytime.

The climatology of vertical velocity profiles and, accordingly, of the GMS characteristics changes from one region to another across tropical oceans (Back and Bretherton 2006). Regional variability in free-tropospheric convergence from the present dataset was studied previously and was found to be rather small (Masunaga 2013). The temporal evolution of the MSE budget parameters and GMS are also qualitatively insensitive to the choice of region when broken down geographically, although the background level of MSE divergence is somewhat lower in the eastern Pacific where large-scale vertical motion climatologically does not reach as high as in the rest of the tropics (not shown). Clear regionality is absent in the temporal variability presumably because the composite time series is constructed around the occurrence of organized convective systems. Even though the vertical velocity profiles are climatologically bottom heavy in the tropical eastern Pacific, occasional intrusions of disturbances there may temporarily destabilize the troposphere through its entire depth. Such cases may be preferentially sampled in the current composite analysis, leading to a potential underrepresentation of the regional climatology.

The results could depend also on the horizontal scale of interest. Horizontal MSE advection ($\mathbf{v} \cdot \nabla h$) was found to be minimal throughout, leaving the MSE transport due to wind divergence ($h\nabla \cdot \mathbf{v}$), which is equivalent to the vertical MSE advection when integrated over the troposphere, to be responsible for MSE import or export. This is because the horizontal moisture field, as an ensemble of many convective events, is nearly uniform within the 100-km-radius domain currently analyzed. Note that this scale is comparable in size to a single grid box typical of climate models and global assimilation models and is chosen to be barely large enough to encompass a mature mesoscale convective system (Houze 2004) so it represents large-scale dynamics but yet retains a close physical relevance to the convective processes at work inside. Horizontal moisture gradients can be larger while convergence generally weakens as the horizontal scale increases, and as a result horizontal MSE advection would be comparable to or may even overwhelm the vertical advection over a sufficiently large domain. This is indeed what is observed in reanalysis datasets (Back and Bretherton 2006) and climate models (Maloney 2009), where the horizontal scale of interest should be at least a few times as large as the grid resolution. This scale dependence could raise a terminological ambiguity in the definition of “large scale” and should be addressed elsewhere.

Acknowledgments. The authors thank Johnny Luo and Yu Xie for their comments on an early version of this work. The TRMM PR (2A25) dataset was provided by the Japan Aerospace Exploration Agency (JAXA); the GPROF 2010 precipitation product by Colorado State University (rain.atmos.colostate.edu/RAINMAP10); the AMSR-E CWV and SST product by Remote Sensing Systems (www.remss.com); the CloudSat 2B-CLDCLASS, 2B-FLXHR-LIDAR, and 2C-PRECIP-COLUMN datasets by the CloudSat Data Processing Center (www.cloudsat.cira.colostate.edu); QuikSCAT SeaWinds ocean wind vector data by the Physical Oceanography Distributed Active Archive Center (PO.DAAC) at the NASA Jet Propulsion Laboratory (podaac.jpl.nasa.gov); and the AIRS/AMSU product by the Goddard Earth Sciences (GES) Data and Information Services Center (DISC; disc.sci.gsfc.nasa.gov). This work is supported by the Japan Society for the Promotion of Science (JSPS) Grant-in-Aid for Young Scientists (23740351) and for Challenging Exploratory Research (26610150).

REFERENCES

- Back, L. E., and C. S. Bretherton, 2006: Geographic variability in the export of moist static energy and vertical motion profiles in the tropical Pacific. *Geophys. Res. Lett.*, **33**, L17810, doi:10.1029/2006GL026672.
- Bretherton, C. S., and A. H. Sobel, 2002: A simple model of a convectively coupled Walker circulation using the weak temperature gradient approximation. *J. Climate*, **15**, 2907–2920, doi:10.1175/1520-0442(2002)015<2907:ASMOAC>2.0.CO;2.
- , P. N. Blossey, and M. Khairoutdinov, 2005: An energy-balance analysis of deep convective self-aggregation above uniform SST. *J. Atmos. Sci.*, **62**, 4273–4292, doi:10.1175/JAS3614.1.
- Brümmer, B., E. Augstein, and H. Riehl, 1974: On the low-level wind structure in the Atlantic trade. *Quart. J. Roy. Meteor. Soc.*, **100**, 109–121, doi:10.1002/qj.49710042310.
- Fulton, S. R., and W. H. Schubert, 1985: Vertical normal mode transforms: Theory and application. *Mon. Wea. Rev.*, **113**, 647–658, doi:10.1175/1520-0493(1985)113<0647:VNMTTA>2.0.CO;2.
- Haertel, P. T., and G. N. Kiladis, 2004: Dynamics of 2-day equatorial waves. *J. Atmos. Sci.*, **61**, 2707–2721, doi:10.1175/JAS3352.1.
- , —, A. Denno, and T. M. Rickenbach, 2008: Vertical-mode decompositions of 2-day waves and the Madden-Julian oscillation. *J. Atmos. Sci.*, **65**, 813–833, doi:10.1175/2007JAS2314.1.
- Handlos, Z. J., and L. E. Back, 2014: Estimating vertical motion profile shape within tropical weather states over the oceans. *J. Climate*, doi:10.1175/JCLI-D-13-00602.1, in press.
- Haynes, J. M., T. S. L'Ecuyer, G. L. Stephens, S. D. Miller, C. Mitrescu, N. B. Wood, and S. Tanelli, 2009: Rainfall retrieval over the ocean with spaceborne W-band radar. *J. Geophys. Res.*, **114**, D00A22, doi:10.1029/2008JD009973.
- Held, I. M., and B. J. Hoskins, 1985: Large-scale eddies and the general circulation of the troposphere. *Advances in Geophysics*, Vol. 28, Academic Press, 3–31, doi:10.1016/S0065-2687(08)60218-6.
- Henderson, D. S., T. S. L'Ecuyer, G. Stephens, P. Partain, and M. Sekiguchi, 2013: A multisensor perspective on the radiative impacts of clouds and aerosols. *J. Appl. Meteor. Climatol.*, **52**, 853–871, doi:10.1175/JAMC-D-12-025.1.
- Hohenegger, C., and B. Stevens, 2013: Preconditioning deep convection with cumulus congestus. *J. Atmos. Sci.*, **70**, 448–464, doi:10.1175/JAS-D-12-089.1.
- Houze, R. A., Jr., 1982: Cloud clusters and large-scale vertical motions in the tropics. *J. Meteor. Soc. Japan*, **60**, 396–410.
- , 2004: Mesoscale convective systems. *Rev. Geophys.*, **42**, RG4003, doi:10.1029/2004RG000150.
- Johnson, R. H., T. M. Rickenbach, S. A. Rutledge, P. E. Ciesielski, and W. H. Schubert, 1999: Trimodal characteristics of tropical convection. *J. Climate*, **12**, 2397–2418, doi:10.1175/1520-0442(1999)012<2397:TCOTC>2.0.CO;2.
- , P. E. Ciesielski, and J. A. Cotturone, 2001: Multiscale variability of the atmospheric mixed layer over the western Pacific warm pool. *J. Atmos. Sci.*, **58**, 2729–2750, doi:10.1175/1520-0469(2001)058<2729:MVOTAM>2.0.CO;2.
- Khouider, B., and A. J. Majda, 2006: A simple multicloud parameterization for convectively coupled tropical waves. Part I: Linear analysis. *J. Atmos. Sci.*, **63**, 1308–1323, doi:10.1175/JAS3677.1.
- Kuang, Z., 2008a: A moisture-stratiform instability for convectively coupled waves. *J. Atmos. Sci.*, **65**, 834–854, doi:10.1175/2007JAS2444.1.
- , 2008b: Modeling the interaction between cumulus convection and linear gravity waves using a limited-domain cloud system-resolving model. *J. Atmos. Sci.*, **65**, 576–591, doi:10.1175/2007JAS2399.1.
- , 2011: The wavelength dependence of the gross moist stability and the scale selection in the instability of column-integrated moist static energy. *J. Atmos. Sci.*, **68**, 61–74, doi:10.1175/2010JAS3591.1.
- Kummerow, C. D., and Coauthors, 2001: The evolution of the Goddard Profiling Algorithm (GPROF) for rainfall estimation from passive microwave sensors. *J. Appl. Meteor.*, **40**, 1801–1820, doi:10.1175/1520-0450(2001)040<1801:TEOTGP>2.0.CO;2.
- , S. Ringerud, J. Crook, D. Randel, and W. Berg, 2011: An observationally generated a priori database for microwave rainfall retrievals. *J. Atmos. Oceanic Technol.*, **28**, 113–130, doi:10.1175/2010JTECHA1468.1.
- Large, W. G., J. C. McWilliams, and S. C. Doney, 1994: Oceanic vertical mixing: A review and a model with a nonlocal boundary layer parameterization. *Rev. Geophys.*, **32**, 363–403, doi:10.1029/94RG01872.
- L'Ecuyer, T. S., N. B. Wood, T. Haladay, G. L. Stephens, and P. W. Stackhouse Jr., 2008: Impact of clouds on atmospheric heating based on the R04 CloudSat fluxes and heating rates data set. *J. Geophys. Res.*, **113**, D00A15, doi:10.1029/2008JD009951.
- Lin, X., and R. H. Johnson, 1996: Kinematic and thermodynamic characteristics of the flow over the western Pacific warm pool during TOGA COARE. *J. Atmos. Sci.*, **53**, 695–715, doi:10.1175/1520-0469(1996)053<0695:KATCOT>2.0.CO;2.
- Majda, A. J., and M. G. Shefter, 2001: Models for stratiform instability and convectively coupled waves. *J. Atmos. Sci.*, **58**, 1567–1584, doi:10.1175/1520-0469(2001)058<1567:MFSIAC>2.0.CO;2.
- Maloney, E. D., 2009: The moist static energy budget of a composite tropical intraseasonal oscillation in a climate model. *J. Climate*, **22**, 711–729, doi:10.1175/2008JCLI2542.1.

- Manabe, S., and J. Smagorinsky, 1967: Simulated climatology of a general circulation model with a hydrological cycle II. Analysis of the tropical atmosphere. *Mon. Wea. Rev.*, **95**, 155–169, doi:10.1175/1520-0493(1967)095<0155:SCOAGC>2.3.CO;2.
- Mapes, B. E., 2000: Convective inhibition, subgrid-scale triggering energy, and stratiform instability in a toy tropical wave model. *J. Atmos. Sci.*, **57**, 1515–1535, doi:10.1175/1520-0469(2000)057<1515:CISSTE>2.0.CO;2.
- , and R. A. Houze Jr., 1995: Diabatic divergence profiles in western Pacific mesoscale convective systems. *J. Atmos. Sci.*, **52**, 1807–1828, doi:10.1175/1520-0469(1995)052<1807:DDPIWP>2.0.CO;2.
- , and P. Zuidema, 1996: Radiative-dynamical consequences of dry tongues in the tropical troposphere. *J. Atmos. Sci.*, **53**, 620–638, doi:10.1175/1520-0469(1996)053<0620:RDCODT>2.0.CO;2.
- Masunaga, H., 2012: A satellite study of the atmospheric forcing and response to moist convection over tropical and subtropical oceans. *J. Atmos. Sci.*, **69**, 150–167, doi:10.1175/JAS-D-11-016.1.
- , 2013: A satellite study of tropical moist convection and environmental variability: A moisture and thermal budget analysis. *J. Atmos. Sci.*, **70**, 2443–2466, doi:10.1175/JAS-D-12-0273.1.
- Neelin, J. D., and I. M. Held, 1987: Modeling tropical convergence based on the moist static energy budget. *Mon. Wea. Rev.*, **115**, 3–12, doi:10.1175/1520-0493(1987)115<0003:MTCBOT>2.0.CO;2.
- , and J.-Y. Yu, 1994: Modes of tropical variability under convective adjustment and the Madden–Julian oscillation. Part I: Analytical theory. *J. Atmos. Sci.*, **51**, 1876–1894, doi:10.1175/1520-0469(1994)051<1876:MOTVUC>2.0.CO;2.
- , and N. Zeng, 2000: A quasi-equilibrium tropical circulation model—Formulation. *J. Atmos. Sci.*, **57**, 1741–1766, doi:10.1175/1520-0469(2000)057<1741:AQETCM>2.0.CO;2.
- Nitta, T., 1970: A study of generation and conversion of eddy available potential energy in the tropics. *J. Meteor. Soc. Japan*, **48**, 524–528.
- , 1972: Energy budget of heat disturbances over the Marshall Islands during the years of 1956 and 1958. *J. Meteor. Soc. Japan*, **50**, 71–84.
- Perry, K. L., 2001: SeaWinds on QuikSCAT level 3 daily, gridded ocean wind vectors (JPL SeaWinds project) version 1.1. JPL Doc. D-20335, Jet Propulsion Laboratory, 39 pp. [Available online at <http://podaac.jpl.nasa.gov>.]
- Peters, M. E., and C. S. Bretherton, 2006: Structure of tropical variability from a vertical mode perspective. *Theor. Comput. Fluid Dyn.*, **20**, 501–524, doi:10.1007/s00162-006-0034-x.
- , Z. Kuang, and C. C. Walker, 2008: Analysis of atmospheric energy transport in ERA-40 and implications for simple models of the mean tropical circulation. *J. Climate*, **21**, 5229–5241, doi:10.1175/2008JCLI2073.1.
- Randall, D. A., Harshvardhan, and D. A. Dazlich, 1991: Diurnal variability of the hydrologic cycle in a general circulation model. *J. Atmos. Sci.*, **48**, 40–62, doi:10.1175/1520-0469(1991)048<0040:DVOTHC>2.0.CO;2.
- Raymond, D. J., 2000: Thermodynamic control on tropical rainfall. *Quart. J. Roy. Meteor. Soc.*, **126**, 889–898, doi:10.1002/qj.49712656406.
- , and Ž. Fuchs, 2007: Convectively coupled gravity and moisture modes in a simple atmospheric model. *Tellus*, **59A**, 627–640, doi:10.1111/j.1600-0870.2007.00268.x.
- , and —, 2009: Moisture modes and the Madden–Julian oscillation. *J. Climate*, **22**, 3031–3046, doi:10.1175/2008JCLI2739.1.
- , S. L. Sessions, and Ž. Fuchs, 2007: A theory for the spinup of tropical depressions. *Quart. J. Roy. Meteor. Soc.*, **133**, 1743–1754, doi:10.1002/qj.125.
- , —, A. H. Sobel, and Ž. Fuchs, 2009: The mechanics of gross moist stability. *J. Adv. Model. Earth Syst.*, **1**, 9, doi:10.3894/JAMES.2009.1.9.
- Riehl, H., and J. S. Malkus, 1958: On the heat balance in the equatorial trough zone. *Geophysica*, **6**, 503–538.
- Sessions, S. L., S. Sugaya, D. J. Raymond, and A. H. Sobel, 2010: Multiple equilibria in a cloud-resolving model using the weak temperature gradient approximation. *J. Geophys. Res.*, **115**, D12110, doi:10.1029/2009JD013376.
- Sobel, A. H., and H. Gildor, 2003: A simple time-dependent model of SST hot spots. *J. Climate*, **16**, 3978–3992, doi:10.1175/1520-0442(2003)016<3978:ASTMOS>2.0.CO;2.
- , and J. D. Neelin, 2006: The boundary layer contribution to intertropical convergence zones in the quasi-equilibrium tropical circulation model framework. *Theor. Comput. Fluid Dyn.*, **20**, 323–350, doi:10.1007/s00162-006-0033-y.
- Stevens, B., J. Duan, M. M. J. C. McWilliams, and J. D. Neelin, 2002: Entrainment, Rayleigh friction, and boundary layer winds over the tropical Pacific. *J. Climate*, **15**, 30–44, doi:10.1175/1520-0442(2002)015<0030:ERFABL>2.0.CO;2.
- Su, H., and J. D. Neelin, 2002: Teleconnection mechanisms for tropical Pacific descent anomalies during El Niño. *J. Atmos. Sci.*, **59**, 2694–2712, doi:10.1175/1520-0469(2002)059<2694:TMFTPD>2.0.CO;2.
- Sugiyama, M., 2009a: The moisture mode in the quasi-equilibrium tropical circulation model. Part I: Analysis based on the weak temperature gradient approximation. *J. Atmos. Sci.*, **66**, 1507–1523, doi:10.1175/2008JAS2690.1.
- , 2009b: The moisture mode in the quasi-equilibrium tropical circulation model. Part II: Nonlinear behavior on an equatorial β plane. *J. Atmos. Sci.*, **66**, 1525–1542, doi:10.1175/2008JAS2691.1.
- Susskind, J., C. D. Barnet, and J. M. Blaisdell, 2003: Retrieval of atmospheric and surface parameters from AIRS/AMSU/HSB data in the presence of clouds. *IEEE Trans. Geosci. Remote Sens.*, **41**, 390–409, doi:10.1109/TGRS.2002.808236.
- , J. M. Blaisdell, L. Iredell, and F. Keita, 2011: Improved temperature sounding and quality control methodology using AIRS/AMSU data: The AIRS Science Team version 5 retrieval algorithm. *IEEE Trans. Geosci. Remote Sens.*, **49**, 883–907, doi:10.1109/TGRS.2010.2070508.
- Thompson, R. M., S. W. Payne, E. E. Recker, and R. J. Reed, 1979: Structure and properties of synoptic-scale wave disturbances in the intertropical convergence zone of the eastern Atlantic. *J. Atmos. Sci.*, **36**, 53–72, doi:10.1175/1520-0469(1979)036<0053:SAPOSS>2.0.CO;2.
- TRMM PR Team, 2005: Tropical Rainfall Measuring Mission (TRMM) Precipitation Radar algorithm. Instruction manual for version 6. Japan Aerospace Exploration Agency and National Aeronautics and Space Administration, 175 pp. [Available online at http://www.eorc.jaxa.jp/TRMM/index_e.htm.]
- Waite, M. L., and B. Khouider, 2009: Boundary layer dynamics in a simple model for convectively coupled gravity waves. *J. Atmos. Sci.*, **66**, 2780–2795, doi:10.1175/2009JAS2871.1.
- , and —, 2010: The deepening of tropical convection by congestus preconditioning. *J. Atmos. Sci.*, **67**, 2601–2615, doi:10.1175/2010JAS3357.1.
- Wang, Z., and K. Sassen, 2001: Cloud type and macrophysical property retrieval using multiple remote sensors. *J. Appl.*

- Meteor.*, **40**, 1665–1682, doi:[10.1175/1520-0450\(2001\)040<1665:CTAMPR>2.0.CO;2](https://doi.org/10.1175/1520-0450(2001)040<1665:CTAMPR>2.0.CO;2).
- Wentz, F. J., and T. Meissner, 2000: AMSR ocean algorithm. Algorithm Theoretical Basis Doc., Remote Sensing Systems, 59 pp. [Available online at <http://www.ssmi.com/>.]
- Wu, Z., 2003: A shallow CISK, deep equilibrium mechanism for the interaction between large-scale convection and large-scale circulations in the tropics. *J. Atmos. Sci.*, **60**, 377–392, doi:[10.1175/1520-0469\(2003\)060<0377:ASCDEM>2.0.CO;2](https://doi.org/10.1175/1520-0469(2003)060<0377:ASCDEM>2.0.CO;2).
- , E. S. Sarachik, and D. S. Battisti, 2000: Vertical structure of convective heating and the three-dimensional structure of the forced circulation on an equatorial beta plane. *J. Atmos. Sci.*, **57**, 2169–2187, doi:[10.1175/1520-0469\(2000\)057<2169:VSOCHA>2.0.CO;2](https://doi.org/10.1175/1520-0469(2000)057<2169:VSOCHA>2.0.CO;2).
- Yanai, M., S. Esbensen, and J.-H. Chu, 1973: Determination of bulk properties of tropical cloud clusters from large-scale heat and moisture budgets. *J. Atmos. Sci.*, **30**, 611–627, doi:[10.1175/1520-0469\(1973\)030<0611:DOBPOT>2.0.CO;2](https://doi.org/10.1175/1520-0469(1973)030<0611:DOBPOT>2.0.CO;2).
- , J.-H. Chu, T. E. Stark, and T. Nitta, 1976: Response of deep and shallow tropical maritime cumuli to large-scale processes. *J. Atmos. Sci.*, **33**, 976–991, doi:[10.1175/1520-0469\(1976\)033<0976:RODAST>2.0.CO;2](https://doi.org/10.1175/1520-0469(1976)033<0976:RODAST>2.0.CO;2).
- Yasunaga, K., and Coauthors, 2006: Melting layer cloud observed during R/V *Mirai* cruise MR01-K05. *J. Atmos. Sci.*, **63**, 3020–3032, doi:[10.1175/JAS3779.1](https://doi.org/10.1175/JAS3779.1).
- Yu, J.-Y., C. Chou, and J. D. Neelin, 1998: Estimating the gross moist stability of the tropical atmosphere. *J. Atmos. Sci.*, **55**, 1354–1372, doi:[10.1175/1520-0469\(1998\)055<1354:ETGMSSO>2.0.CO;2](https://doi.org/10.1175/1520-0469(1998)055<1354:ETGMSSO>2.0.CO;2).